Measurements of the dynamic structure factor near the lambda temperature in liquid helium*

J. A. Tarvin,[†] F. Vidal,[‡] and T. J. Greytak

Department of Physics and Center for Materials Science and Engineering, Massachusetts Institute of Technology, Cambridge, Massachusetts 02139

(Received 27 December 1976)

The dynamic structure factor $S(q,\omega)$ was measured by Brillouin scattering in liquid ^{4}He at $q = 1.79 \times 10^5$ cm^{-1}. Results were obtained at two densities: $\rho = 0.175$ g/cm^3 for which $P_\lambda = 23.1$ bars and $\rho = 0.179$ g/cm^3 for which $P_\lambda = 28.5$ bars. Values of the reduced temperature $\epsilon \equiv (T - T_\lambda)/T_\lambda$ varied from -5×10^{-2} to -5×10^{-6} and from 1.3×10^{-5} to 5×10^{-2}. This range involves both the hydrodynamic and the critical regions; values of $q\xi$ fall between 5×10^{-2} and 21 below T_λ and between 4.5 and 2×10^{-2} above T_λ. This article presents the data on the critical mode, which is second sound below the transition and heat diffusion above. The most striking result is that the damping of the critical mode is essentially independent of ϵ over the entire range of temperatures studied. This behavior is qualitatively different from the strong temperature dependence, consistent with dynamic scaling, which is observed at low frequencies. On the other hand, any dispersion in the velocity of high frequency ($\sim$ several MHz) second sound, if present, is less than 2%. $S(q,\omega)$ retains a two-peaked structure well into the critical region below T_λ; it still appears in the measured spectra (which contain the instrumental width as well) at $q\xi \sim 4$. At T_λ and in the critical region just above, there is evidence for a non-Lorentzian shape of $S(q,\omega)$. The critical mode contribution to $S(q,\omega)$ is compared with a theoretical calculation of Hohenberg, Siggia, and Halperin based on the planar-spin model of ^{4}He. The theory matches both the overall width and the general features of the shape of $S(q,\omega)$ to within our spectral resolution at T_λ. However, closer to $q\xi = 1$ in the critical region, and in the hydrodynamic regions both above and below T_λ, the theory predicts linewidths which are too small.

I. INTRODUCTION

The modern definition of a second-order phase transition is expressed in terms of the behavior of some "order parameter" in the system. The mean value of this order parameter is finite below the transition temperature T_c, goes smoothly to zero at $T = T_c$, and is zero for $T > T_c$. The fluctuations in the order parameter, however, diverge at the transition. In such systems many of the thermodynamic parameters which couple to the order parameter diverge or go to zero with some power-law dependence on $|T - T_c|$. There is also a characteristic length associated with the phase transition, the correlation length $\xi(T)$ for fluctuations in the order parameter, which diverges as the transition is approached. These effects are collectively referred to as "critical phenomena"; they have been extensively studied experimentally and theoretically in a wide variety of systems.[1]

Often one is interested in the dynamics of one spatial Fourier component, with wave vector q, of some quantity such as magnetization or density. In most experiments $q\xi$ is much less than 1. In these cases the equations of hydrodynamics apply, although the hydrodynamic parameters may exhibit the strong temperature dependences mentioned above. Very close to the transition, where $q\xi \gtrsim 1$, the situation becomes more complicated.

The equations of hydrodynamics no longer apply since they assume that the spatial distances involved are all much larger than any characteristic length associated with the medium. A similar situation occurs in a gas when the density is lowered to the point where the mean free path of the molecules is comparable to the wavelength of sound. In this system, which does not involve critical phenomena, one is able to resort to kinetic theory—the Boltzmann equation—to describe analytically the behavior of sound in the dilute limit. Near a second-order phase transition the characteristic length of importance in the medium is not the mean free path of the molecules, but $\xi(T)$, and the appropriate equations of motion in the critical region, where $q\xi \lesssim 1$, are not completely understood. Therefore, experiments done in the critical region probe not only the parameters describing the medium, but the equations of motion themselves.

Detailed studies of the dynamics inside the critical region have only been carried out for a few systems. They differ, among other things, in the number of components n in the order parameter.[2] In the isotropic antiferromagnet RbMnF$_3$ studied by Lau *et al.*,[3] the order parameter is the staggered magnetization which has three equivalent spatial components, so $n = 3$. In the uniaxial antiferromagnet MnF$_2$ studied by Schulhof *et al.*,[4] the order parameter is the staggered magnetization

along the easy axis, and $n = 1$. The gas-liquid critical point and the binary mixture consolute point are mathematically similar and have $n = 1$, the order parameter being the density difference or concentration difference in the two phases below T_c. These two systems have been studied in the critical region by a number of workers, and this work has been discussed by Swinney and Henry.[5]

We present here experimental results on the dynamics of density fluctuations near the λ transition in liquid ^{4}He, for both the hydrodynamic and the critical regions. The order parameter associated with the λ transition is a complex quantity[6,7] $\psi = \psi_0 e^{i\phi}$ which is related to the expected value of the condensate wave function: the superfluid velocity is given by $\vec{v}_s = (\hbar/m)\nabla\phi$, and the number of atoms in the zero-momentum state is proportional to ψ_0^2. Unfortunately, ψ is not measurable directly; it is only observable through its coupling to the density fluctuations. From the point of view of understanding dynamical critical phenomena, a study of the lambda transition offers several advantages. Since ψ is a complex scalar, n equals two, so ^{4}He provides a case not previously studied experimentally. In addition, the critical mode is propagating in the condensed phase but diffusive in the normal phase; this situation is shared only by the isotropic antiferromagnet and offers a richer range of possible dynamic behavior than is available in other systems. For the uniaxial antiferromagnet, gas-liquid and binary mixture systems the critical mode is diffusive both above and below the transition. Finally, studies of the λ transition as a function of pressure allow one to check the predictions of the hypothesis of universality.[8]

Light scattering is a particularly useful method for studying the critical region associated with the λ transition because $\xi(T)$ becomes comparable to the wavelength being studied $(2\pi/q)$ at accessible temperature differences. In our experiments, $q\xi \sim 1$ at $T - T_\lambda \sim -1$ mK, whereas in most conventional experiments the dimension of the probe is large compared to ξ over all of the accessible temperature range. For example, in the experiments of Tyson on driven second sound[9,10] $q\xi$ was about 10^{-2} at the shortest wavelength (0.02 cm) and the smallest value of $T - T_\lambda$ (-10^{-4} K) studied.

In this experiment we use Brillouin scattering to measure the dynamic structure factor[11] $S(q, \omega)$, the space and time Fourier transform of the density correlation function. q is the wave vector of the fluctuation being studied; it is determined by the scattering angle θ, the vacuum wave vector of the incident light q_0, and the index of refraction of the helium n_r:

$$q = 2q_0 n_r \sin(\tfrac{1}{2}\theta) . \tag{1}$$

ω is the angular frequency shift of the scattered light. At a given value of q, $S(q, \omega)$ is the power spectrum of the spontaneous fluctuations in the amplitude of that spatial Fourier component of the density which has wave vector q. In our experiment, $S(q, \omega)$ consists of two distinct parts. The first, $S_1(q, \omega)$, is primarily due to pressure fluctuations at constant entropy. These fluctuations propagate as a sound wave (first sound) with velocity u_1, causing $S_1(q, \omega)$ to be peaked at $\omega = \pm u_1 q$. The other contribution to the spectrum, $S_2(q, \omega)$, is primarily due to entropy fluctuations at constant pressure. Above T_λ, this is a diffusive mode, and S_2 consists of a single Lorentzian centered at $\omega = 0$. A unique feature of liquid helium is that, in the superfluid phase, the entropy fluctuations propagate as a wave (second sound) with velocity u_2. Below T_λ, therefore, S_2 consists of a pair of lines at $\omega = \pm u_2 q$. Both above and below T_λ, S_1 and S_2 are well separated. S_2 is negligible at the relatively large frequency shift, $u_1 q$; and S_1 is negligible at the much smaller shift, $u_2 q$.

Ideally, one would like to measure the spectrum of the order-parameter fluctuations in helium directly, but this is not possible since ψ is not a measurable quantity. However, Hohenberg[12] has shown that second sound dominates the spectrum of order-parameter fluctuations close to the transition. So second sound is the critical mode for the λ transition, and $S_2(q, \omega)$ contains most of the information about the dynamics of the critical fluctuations. Unfortunately, the scattering associated with S_2 is much less than that from S_1 under ordinary circumstances. The first discussion of the spectrum of light scattered from superfluid ^{4}He was published by Ginzburg[13] in 1943, and he was able to calculate the ratio of the intensities due to first and second sound. The correct expression for I_2/I_1 was complicated, but he pointed out that it could be approximated by

$$I_2/I_1 = \gamma - 1 . \tag{2}$$

Here I_i is the integrated intensity of S_i and $\gamma = C_P/C_V$ is the specific-heat ratio. It is now recognized[14,15] that this is an excellent approximation in all regions of the phase diagram where the hydrodynamic equations are expected to apply. The ratio given by Eq. (2) is very small at saturated vapor pressure, making the scattering from second sound very weak compared to that from first sound. However, $\gamma - 1$ increases with pressure near the λ line. Therefore, the scattering from second sound is enhanced at higher pressures. This was first noted by Ferrell et al.[6] who also pointed out that close to T_λ one should observe the effects of critical fluctuations on $S(q, \omega)$. It is for this reason that the present experiments were

carried out at elevated pressures, where $I_2/I_1 \sim \frac{1}{2}$, rather than at saturated vapor pressure, where I_2/I_1 peaks at about 10^{-2}.

The earliest Brillouin experiments in helium studied the dispersion and attenuation of first sound[16,17] and the properties of ^{3}He-^{4}He mixtures.[18-20] Later experiments have concentrated on ^{4}He near the λ transition.[21-27] In this paper we present our most recent measurements of $S_2(q, \omega)$. Our results for first sound will be given in a subsequent paper. In Sec. II we present the hydrodynamic form of $S(q, \omega)$ and outline the theory for $S(q, \omega)$ in the critical region. In Sec. III the experimental apparatus and procedures are described. Section IV contains a discussion of the methods used to analyze the data. In Sec. V we compare our measured spectra with the hydrodynamic form, with a simple model which allows parametrization of the spectra at all temperatures, and with spectra calculated[28] from the symmetric planar-spin model by the renormalization-group approach.

II. THEORY

A. Hydrodynamic spectrum

In order to calculate $S(q, \omega)$, one must know the temporal behavior of the fluctuations about equilibrium. To determine this, one employs the Onsager "regression of fluctuations" hypothesis,[29] a version of the fluctuation-dissipation theorem, which states that the time dependence of the equilibrium correlation function for the amplitude of the qth Fourier component of the density is the same as the time evolution of an externally induced density disturbance of wave vector q which is released at $t = 0$. The latter macroscopic quantity can be calculated from the hydrodynamic equations of motion of the system. The details of this type of calculation for classical fluids have been given by Mountain.[30] In the case of superfluid ^{4}He the equations of two-fluid hydrodynamics are well understood[31] and go over smoothly to the equations governing a simple classical fluid when the superfluid fraction ρ_s/ρ goes to zero. Calculations of the full frequency dependence of $S(q, \omega)$ for liquid ^{4}He have been carried out by Vinen,[32] Hohenberg,[15] and Holmes.[33] The theory of Brillouin scattering from liquid helium has recently been reviewed by Stephen.[34]

The spectrum consists of two parts, $S_1(q, \omega)$ due to first sound and $S_2(q, \omega)$ due to second sound. Both parts have exactly the same functional dependence on[33] ω:

$$S_i(q, \omega) \propto \frac{a_i + b_i \omega^2}{(c_i^2 - \omega^2)^2 + d_i \omega^2} . \tag{3}$$

In general, the spectral parameters in these expressions (a_i, b_i, c_i, and d_i) depend in a complicated way on the thermodynamic parameters and on the wave vector q. In various limiting cases, however, they are given by simple explicit expressions. For instance, in our experiments the frequency shift associated with first sound is always much greater than that due to second sound, but the second sound shift may be as small as the spectral width due to damping. Under these circumstances, near the first sound peaks, $S_1(q, \omega)$ is well approximated by

$$S_1(q, \omega) = \frac{A}{\pi \gamma} \frac{2\Gamma_1 \omega_1^2}{(\omega_1^2 - \omega^2)^2 + 4\Gamma^2 \omega^2} . \tag{4}$$

This can be written as a sum of Lorentzian and dispersive line shapes centered exactly at the frequencies $\omega = \pm \omega_1 = \pm u_1 q$:

$$S_1(q, \omega) = \frac{A}{2\pi\gamma} \left(\frac{\Gamma_1}{(\omega - \omega_1)^2 + \Gamma_1^2} - \frac{\Gamma_1}{\omega_1} \frac{\omega - \omega_1}{(\omega - \omega_1)^2 + \Gamma_1^2} + \frac{\Gamma_1}{(\omega + \omega_1)^2 + \Gamma_1^2} + \frac{\Gamma_1}{\omega_1} \frac{\omega + \omega_1}{(\omega + \omega_1)^2 + \Gamma_1^2} \right) , \tag{5}$$

where

$$\omega_1 = u_1 q ,$$

$$\Gamma_1 = \tfrac{1}{2} D_1 q^2 = \tfrac{1}{2}(1/\rho)(\tfrac{4}{3}\eta + \zeta_2) q^2 , \tag{6}$$

$$A = k_B T \rho^2 \beta_T ,$$

and the dissipative terms (kinetic coefficients) such as η and ζ_2 have their conventional meanings.[31] Note that the dispersive functions peak at $|\omega - \omega_1| = \Gamma_1$, and at those points the ratio of the magnitudes of the dispersive to the Lorentzian parts is Γ_1/ω_1. In these experiments the maximum value of Γ_1/ω_1 is about 0.01, so the dispersive parts of $S_1(q, \omega)$ may be neglected. These expressions

show that there are two quantities that can be obtained from measurements of S_1: the velocity u_1 and the damping constant D_1 of first sound.

As long as the frequency shift of first sound is much greater than either the second sound shift or any of the linewidths, $S_2(q, \omega)$ is well represented by the expression

$$S_2(q, \omega) = \frac{2A}{\pi} \frac{\gamma - 1}{\gamma} \frac{\Gamma_\zeta \Omega_2^2 + \Gamma_\kappa \omega^2}{(\Omega_2^2 - \omega^2)^2 + 4(\Gamma_\zeta + \Gamma_\kappa)^2 \omega^2} , \tag{7}$$

where

$$\Omega_2^2 = \omega_2^2 + 4\Gamma_\zeta \Gamma_\kappa = (u_2 q)^2 + 4\Gamma_\zeta \Gamma_\kappa ,$$

$$2\Gamma_\kappa = D_\kappa q^2 = \kappa q^2/\rho C_P , \tag{8}$$

and

$$2\Gamma_\zeta = D_\zeta q^2$$

$$= \frac{\rho_s}{\rho_n} \frac{1}{\rho} [(\tfrac{4}{3}\eta + \zeta_2) + \rho^2\zeta_3 - \rho\zeta_1 - \rho\zeta_4] q^2 .$$

Here κ is the thermal conductivity, and C_P is the specific heat per unit mass. The shape of S_2 depends on three parameters: ω_2, Γ_ζ, and Γ_κ. When $\omega_2 \gg \Gamma_\kappa$ and Γ_ζ, Eq. (7) represents a pair of well-resolved peaks at $\omega = \pm\omega_2 = \pm u_2 q$, whose half widths are given by $\Gamma_\zeta + \Gamma_\kappa$. In this case the three parameters have simple physical interpretations in terms of a propagating second sound mode; they are proportional to the velocity u_2 and two separate contributions to the damping D_ζ and D_κ. Closer to T_λ, where $\omega_2 \sim \Gamma_\zeta$ or Γ_κ, the double maximum in $S_2(q, \omega)$ may disappear, and the physical interpretation of the three parameters is less clear. Above T_λ, where $\rho_s/\rho = 0$, both ω_2 and Γ_ζ are zero, and Eq. (7) reduces to a simple Lorentzian line centered at $\omega = 0$ whose half width is $D_\kappa q^2$. Here D_κ regains a simple physical interpretation: the thermal diffusivity in the normal state

$$S_2(q, \omega) = \frac{A}{\pi} \frac{\gamma - 1}{\gamma} \frac{D_\kappa q^2}{\omega^2 + (D_\kappa q^2)^2} . \tag{9}$$

For those values of ω where $S_2(q, \omega)$ is significant, Eq. (4) does not apply, but it can be shown[33] that $S_1(q, \omega)$ has a small constant contribution

$$S_1(q, \omega \approx 0) = \frac{2A}{\pi\gamma} \frac{\Gamma_1 + 2(\gamma - 1)\Gamma_\kappa}{\omega_1^2} . \tag{10}$$

These results for $S(q, \omega)$ neglect relaxation effects which may be present in the helium. In general, if a relaxation with a characteristic time τ couples to the density, $S(q, \omega)$ will contain an additional line centered at $\omega = 0$, whose half width is τ^{-1}. Kretzen and Mikeska[35] have considered the effect of an order-parameter relaxation on the spectrum. They conclude that the effect is negligible in the hydrodynamic region. In an earlier experiment[25] we searched for evidence of such an additional central component with $\tau \sim \xi(T)/u_2(T)$.[12] We found that the effect, if present, was too weak to be observed.

B. Critical behavior

The superfluid density ρ_s is a quantity of central importance in the two fluid hydrodynamics of superfluid ^{4}He; it is also closely related[36] to the order parameter in discussions of the critical behavior of ^{4}He. Direct measurements[37,38] of ρ_s have shown a power-law dependence on the reduced temperature $\epsilon \equiv (T - T_\lambda)/T_\lambda$:

$$\rho_s/\rho \propto |\epsilon|^\zeta . \tag{11}$$

The measured values of ζ were equal to $\tfrac{2}{3}$ within the experimental error. The availability of high-quality specific-heat data then allowed a careful check[39] of the hydrodynamic formula for the second-sound velocity:

$$u_2^2 = (S^2 T'/C_P)(\rho_s/\rho_n) , \tag{12}$$

where S is the entropy. The left- and right-hand sides of Eq. (12) agreed within the combined experimental error. Because of the near logarithmic dependence of C_P on ϵ, u_2^2 is not expected to have precisely a power-law dependence on ϵ; however, if a power law is fit to the data, u_2^2 goes to zero at T_λ with an exponent close to 0.77. Subsequent experiments[40] have assumed the validity of Eq. (12), and used precision measurements of u_2 to study higher-order singular contributions to the temperature dependence of ρ_s and to investigate the question of universality through the pressure dependence. The result is that Eq. (11) is only the leading term in an expansion of ρ_s; however, the asymptotic exponent ζ is still consistent with $\tfrac{2}{3}$ independent of pressure. Scaling laws give an expression[36] for the exponent ζ in terms of an exponent α' which describes the behavior of the specific heat ($\alpha' = 0$ if C_P is logarithmic):

$$\zeta = \tfrac{1}{3}(2 - \alpha') . \tag{13}$$

There is some experimental indication that ζ is slightly greater than $\tfrac{2}{3}$, and this is consistent with the most recent C_P data indicating a very small but negative α'.[41]

The exponent ζ for ρ_s is particularly important for the study of the critical behavior in ^{4}He because another exponent expression[12] derived from static scaling arguments relates it to the exponent ν' for the correlation length below T_λ ($\xi \propto |\epsilon|^{\nu'}$):

$$-\nu' = \zeta . \tag{14}$$

This expression can be checked to some extent[41] through measurements of the depression of T_λ in restricted geometries, an effect which depends on the size of ξ. These measurements give $\nu' \approx -\tfrac{2}{3}$, in agreement with Eq. (14). There is no way to measure the exponent ν for the correlation length above T_λ, but it is usually assumed that $\nu = \nu'$. Although the convention for the exponents in the temperature dependence of $\xi(T)$ is unambiguous, the prefactor depends on the precise way in which $\xi(T)$ is defined in the theory or model being used. In this paper we employ the expressions used by Hohenberg, Siggia, and Halperin[28]:

$$\begin{aligned} \xi_T &= 3.6(-\epsilon)^{-2/3} \text{ Å}, \quad T < T_\lambda , \\ \xi_+ &= 1.4(\epsilon)^{-2/3} \text{ Å}, \quad T > T_\lambda . \end{aligned} \tag{15}$$

Here the subscript T used for $T < T_\lambda$ indicates the

correlation length for transverse fluctuations in ψ, and the subscript + indicates a correlation length defined in a different manner for $T > T_\lambda$.[28]

We are now in a position to discuss the behavior of the various quantities which determine $S_2(q, \omega)$. In the hydrodynamic region, and in the absence of relaxation effects, the velocity of second sound should be independent of frequency and given by Eq. (12). In these Brillouin scattering experiments the second-sound frequency is in the range of 1–20 MHz; but as long as $q\xi < 1$ we see no deviation from measured low-frequency values of u_2.[40]

Dynamic scaling predicts[6,7] that the damping constant for second sound $D_2 \equiv D_\kappa + D_\zeta$ is given by

$$D_2 = a u_2 \xi , \qquad (16)$$

where a is a numerical constant of order unity. If the temperature dependence of the specific heat in Eq. (12) is neglected, D_2 would be proportional to $|\epsilon|^{-1/3}$; using the best power-law fit to the actual u_2 results mentioned above, D_2 should have an exponent of -0.28. Tyson[9] measured D_2 in the hydrodynamic region at saturated vapor pressure close enough to T_λ that Eq. (16) should apply. He did find a divergent behavior of D_2 with an exponent of -0.34 ± 0.06.

In the hydrodynamic region, and in the absence of relaxation effects, D_2 should be independent of the frequency of the second sound. Tyson verified that this was true over the range of frequencies involved in his experiment: 270–5400 Hz. However, recent Brillouin scattering measurements[24,25,27] in the hydrodynamic region at frequencies of the order of 20 MHz find a D_2 which is essentially temperature independent and is smaller than the values found by Tyson for $T - T_\lambda > -10$ mK. This serious discrepancy has caused concern among both experimenters and theorists, and is as yet unexplained. The experimental work presented here confirms and extends the previous light-scattering results for D_2. The most recent theoretical calculations[28] of D_2 show the temperature dependence predicted by dynamic scaling [Eq. (16)], but give a prefactor which is about five times smaller than that measured by Tyson.

Dynamic scaling also predicts that the dependence of the thermal diffusivity D_κ on $|\epsilon|$ above T_λ should be proportional to the dependence of D_2 on $|\epsilon|$ below T_λ. This was confirmed by Ahlers[42] in careful measurements of the divergence of the thermal conductivity κ near T_λ in the normal state. Our Brillouin scattering measurements of D_κ appear to leave the hydrodynamic region before this critical divergence in κ manifests itself over the noncritical contributions to κ. However, in the hydrodynamic region the D_κ from light

scattering is in excellent agreement with values calculated from measured values of κ and C_P.

When $q\xi \gtrsim 1$, the equations of hydrodynamics no longer apply since they are based on the assumption that there is no characteristic length associated with the liquid. Under these circumstances the general shape of $S(q, \omega)$ will differ from the hydrodynamic form discussed above. Simple dynamic scaling arguments based on the assumption of a single characteristic length are unable to predict the exact form of $S_2(q, \omega)$ in the critical region; however, they do give some information about the q and T dependence of the spectrum.[12] There is a characteristic frequency ω^* which represents the frequency scale or extent of $S_2(q, \omega)$, and it is a homogeneous function of q and $q\xi$:

$$\omega^* = q^z \Omega(q\xi) . \qquad (17)$$

The exponent z is independent of q and ξ; Ω depends only on the product $q\xi$. Since $\omega^* = \omega_2 = q u_2$ in the hydrodynamic region, Ω must be proportional to $(q\xi)^{-1/2}$ there, and z must be $\frac{3}{2}$. The function Ω should go to a limiting value as $q\xi \to \infty$; consequently, ω^* becomes independent of T very close to T_λ, and this limiting extent is proportional to $q^{3/2}$. Dynamic scaling also predicts that $S_2(q, \omega)$ depends on temperature only through the temperature dependence of ξ and ω^*:

$$S_2(q, \omega) = (2\pi/\omega^*)f(q\xi, \omega/\omega^*)S_2(q) . \qquad (18)$$

Here f is a normalized line-shape function, and $S_2(q)$ is the second-sound contribution to the static structure factor. f corresponds to the hydrodynamic form when $q\xi \ll 1$ and approaches some limiting shape when $q\xi \to \infty$. Simple dynamic scaling does not predict the forms of the functions Ω and f. Figure 1 summarizes the expected behavior of $S_2(q, \omega)$ for $T < T_\lambda$. As T approaches T_λ, the frequency shift decreases and the linewidth increases. As $q\xi$ grows very large, $S_2(q, \omega)$ reaches a temperature-independent form. The extent of this limiting form is proportional to $q^{3/2}$, and its shape is expected to differ from the Lorentzian shape predicted by hydrodynamics.

The experiments which we describe here are resolution limited, so we are not able to determine $S_2(q, \omega)$ precisely throughout the critical region. However, we are able, for the first time, to get some information about both the asymptotic ω^* and the limiting spectral shape at T_λ. The q dependence of the spectrum can be seen to be central to the theory of dynamic scaling. The predicted q dependence has been carefully verified for those systems whose behavior inside the critical region has been studied previously.[3-5] Such a study has not been carried out for liquid helium; however,
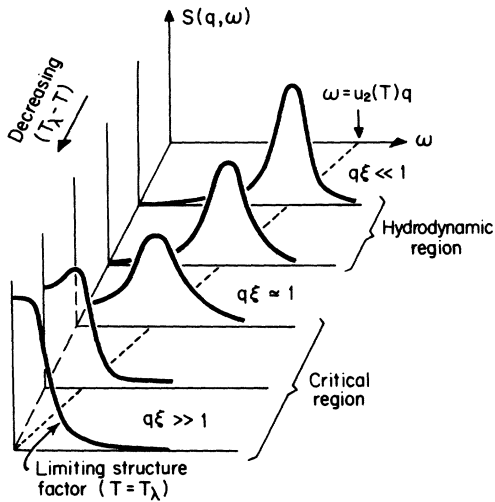
FIG. 1. Schematic representation of the second-sound contribution to $S(q, \omega)$ for $T < T_\lambda$. The contribution from first sound occurs farther out along the ω axis.

a repetition of the present experiments using a uv laser will enable us to measure the q dependence of $S_2(q, \omega)$. Such an experiment would be of particular interest since the damping of second sound in the hydrodynamic region does not appear to follow the hydrodynamic q dependence.

More detailed calculations of the critical dynamics of superfluid helium require the assumption of some model Hamiltonian, and the model which is thought to be appropriate is the planar-spin model in three dimensions.[43] This model ideally represents a three-dimensional easy-plane ferromagnet in which the order parameter is the two-component vector $(n = 2)$ corresponding to the magnetization in the plane. The model is called symmetric when the magnetic field perpendicular to the plane is zero and asymmetric when the perpendicular field is finite. The asymmetric case is the more realistic model for helium since it can represent the strong temperature dependence of the specific heat. Hohenberg, Siggia, and Halperin[28] have recently used renormalization-group methods to calculate $S_2(q, \omega)$ using the symmetric planar-spin model. The resulting spectra contain no adjustable parameters. In Sec. V we make a detailed comparison of these spectra with our experimental results. Very near T_λ the data is resolution limited, but even so the agreement between theory and experiment is surprisingly good. In the hydrodynamic region, however, the theory greatly underestimates the damping of second sound $(T < T_\lambda)$ and the thermal diffusivity $(T > T_\lambda)$. It has been suggested[28] that some of this discrepancy in the hydrodynamic region might be allevi-

ated if the calculations could be carried out for the asymmetric planar-spin model.

III. APPARATUS AND TECHNIQUES

A schematic diagram of the experiment is shown in Fig. 2. Light from a single-mode argon ion laser is passed through the scattering cell located inside a liquid-helium cryostat. The spectrum of the light scattered at 90° is analyzed by a spherical Fabry-Perot interferometer. Since the scattered intensity is very weak, a cooled photomultiplier and single-photon counting methods are used. While a spectrum is being recorded on punched paper tape, the temperature and pressure of the sample are monitored on a strip-chart recorder.

A similar experimental arrangement applied to Brillouin scattering from superfluids has been discussed in detail earlier[20]; however, in the present experiment, we have made two important changes in the apparatus.[33,44] First, the optical resolution has been increased. The intrinsic width (full width at half maximum) of the second sound lines is of the order of 2 MHz and the splitting goes to zero as $T \to T_\lambda$. To allow quantitative measurements of these features of the spectrum, the frequency stability of the laser has been improved, and a new spherical Fabry-Perot interferometer with greater resolving power has been constructed. Second, the temperature stability has been improved. It is important to study the spectrum as close to the λ transition as possible, but the unavoidable absorption of a small amount of laser power in the cell presents a heat leak which makes precise temperature control difficult. Therefore, a new scattering cell has been specifically designed for precision temperature measurement and control.

A. Laser and Fabry-Perot

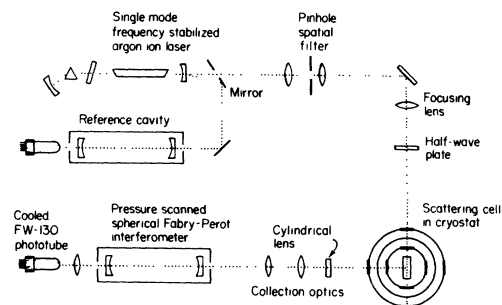A typical gas laser oscillates in several of the longitudinal modes of its resonance cavity simul-

FIG. 2. Experimental arrangement for Brillouin scattering from liquid ^{4}He.

taneously. Although it is now straightforward to eliminate all but one of those modes by using an intracavity etalon,[45] it is difficult to stabilize the frequency of that mode. The plasma tube and solenoid of the laser[46] used in this experiment are cooled by water flowing in the space between them. Since the optical resonator structure is mounted directly on this assembly, vibrations associated with the water (turbulence at high flow rates, boiling at lower rates) cause a modulation of the mirror spacing and alter the laser frequency. In our previous experiments on ^{3}He-^{4}He solutions[20] this effect caused a frequency jitter of about 5 MHz breadth and limited the experimental resolution.

A new, more massive resonator structure has been fabricated from 3.2-cm-diam invar rods and 2.5-cm-thick steel end plates. The original mirror mounts are attached to the new end plates, but the resonator structure and the laser tube assembly now rest separately on a granite slab. Airborne vibrations are diminished by placing the laser in a box lined with acoustic tile and cooled by tap water flowing in finned copper tubing.

The laser frequency is locked to a passive spherical Fabry-Perot reference cavity to eliminate drift and reduce the remaining low-frequency jitter. A new electronic servo with a wider bandwidth (5 kHz) than that used earlier also contributes to the increased stability. The linewidth of the laser is now less than 10% of the total instrumental linewidth. The new Fabry-Perot spectrometer has a spacing of 50.06 cm and a free spectral range of 149.7 MHz. The full width at half height of the instrumental profile of the entire system is 2.9 MHz.

B. Scattering cell

The scattering cell is shown in Fig. 3. It is suspended from the cooling bath and surrounded by vacuum. It is made of oxygen-free high-conductivity copper. The top of the cell is in contact with the pumped ^{4}He cooling bath which extends into a channel around each of the cell's four windows; only two of these channels are shown. This design provides a large area of contact between the cooling bath and the cell, and also minimizes thermal gradients in the copper.

The helium in the cooling bath is, of course, separate from that in the scattering chamber. Inside this chamber a series of apertures along the laser beam axis keeps light scattered by slight, microscopic imperfections in the windows and dirt or films on the window surfaces from reaching the scattering region in the center of the cell. In contrast to helium II (below T_λ), helium I has
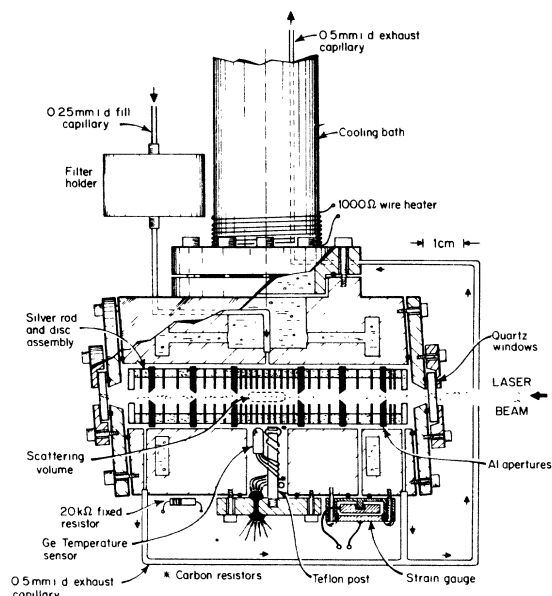

FIG. 3. Scattering cell.

poor thermal conductivity. An array of silver disks connected to the apertures and the cell walls improves thermal homogeneity and decreases the thermal time constant of the helium.

The windows on the laser axis were made from crystalline quartz because of its high thermal conductivity. Since crystalline quartz is both birefringent and optically active,[47] the window surfaces are normal to the optic axis to keep the laser beam linearly polarized. A half-wave plate in front of the cryostat rotates the plane of polarization of the laser beam so that it is vertical in the scattering volume. The windows on earlier cells reflected some of the incident light back into the laser. Even though the reflected power was small, it affected the stability of the laser. A 3° tilt of the windows on the laser axis eliminates this difficulty in the present cell.

C. Sample preparation

In order to eliminate Tyndall scattering, it is important that the sample contain no dust or frozen air. Furthermore, since we wish to take spectra along isochores, the part of the sample volume which is not at the sample temperature (in capillaries, for instance) should be minimized. The sample fill system was designed with these two points in mind. It is shown in Fig. 4.

Ultra-high-purity (99.999%) ^{4}He passes through a liquid nitrogen cold trap and a 0.2-μm millipore filter at room temperature before entering the cryostat through a 0.25-mm-i.d. capillary. The shut-off and safety valves at the entrance to the
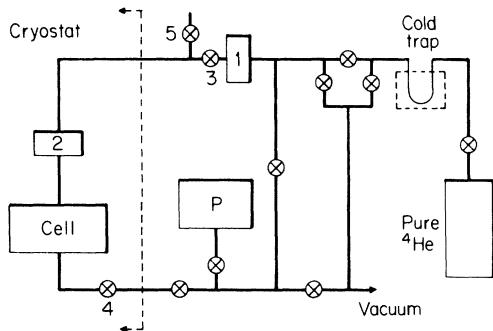
FIG. 4. Sample fill system. 1 and 2 are filters; 3 is a shut-off valve; 4 is a low-temperature valve; 5 is a safety valve which releases at 100 bars.

cryostat are filled with epoxy to minimize dead volume. A 0.02-μm filter connected to the cell prevents dust and frozen air from reaching it, and a 0.5-mm-i.d. capillary connects the cell to a shut-off valve at 4.2 K. The dead volume of the valve is less than 0.02 cm^3. A 1-mm-i.d. capillary goes from there to room temperature. The separate fill and exhaust lines allow us to clean the cell itself by flushing with large quantities of clean helium.

Pressure measurements are calibrated by a 6-in Heise model CMM bourdon tube gauge (P in Fig. 4) with a full-scale reading of 34 atm. Its sensitivity is 0.01 atm and its rated accuracy is 0.034 atm.

D. Measurement of temperature and pressure

Once the inlet and exhaust valves are shut, the sample pressure is measured by the capacitative pressure transducer mounted on the bottom of the cell. The transducer is a strain gauge very similar to that described by Straty and Adams.[48] Its capacitance is measured with a General Radio model 1615A bridge, and the transducer is calibrated with the Heise gauge. The sensitivity of 3 $\times 10^{-5}$ bar is more than adequate for the required measurements.

Three resistance thermometers are used in this experiment. They are inside the scattering chamber so that the sample temperature can be measured directly; their placement is shown in Fig. 3. The principal thermometer is a Cryocal 2500 L germanium resistor. Its resistance is measured in a bridge operated by 92 Hz.[44] It was calibrated *in situ* against the T_{58} vapor-pressure scale of ^{4}He. The power dissipated in it is 6×10^{-9} W and temperature changes of 2 μK can be detected with a time constant of 1 sec.

The second thermometer is a carbon resistor used in the regulation of the sample temperature.

It is located atop the Teflon post; its resistance is also measured in an ac bridge. Refrigeration is provided by pumping on ^{4}He in the cooling bath and coarse temperature regulation is achieved by controlling the vapor pressure with a manostate. The final temperature control is achieved electronically. First, the cooling bath is heated by about 1 mW dissipated in the heater wound around it, and the manostat is set so that the sample is at the desired temperature. Then the bridge for the second thermometer is nulled. Finally, during operation the error signal from this bridge is amplified and used to vary the current in the heater. When the sample is just below T_λ, this two-stage regulator reduces temperature fluctuations to less than 5 μK peak to peak. Just above T_λ, where the thermal conductivity of the helium is very low, the fluctuations are about 15 μK peak to peak with a time constant of several minutes. These figures are indicative of the stability during an experimental run while the laser beam is passing through the cell.

The third thermometer is a carbon resistor used to determine the λ point by a refinement of an indirect measurement of thermal conductivity, first noted by Chase.[49] In a dc Wheatstone bridge the thermometer is heated with 10^{-7} W. The superfluid removes the heat efficiently, but at the λ point the effective thermal conductivity decreases catastrophically. The temperature of the resistor, as measured by the value of its resistance, rises quickly above its surroundings. If the applied power is reduced so that the discontinuity in resistance is just visible, T_λ can be determined within 1 μK. The third thermometer is only used to locate the λ transition; T_λ is actually read on the principal thermometer, the germanium resistor. The precision of this reading is 1 μK, but its accuracy is only about 1 mK. However, it is only the difference $T - T_\lambda$ which must be known on a μK scale, and dT/dR for the germanium resistor is known well enough to assure an accuracy of 1 μK in $T - T_\lambda$. The third resistor is 2.2 cm below the scattering volume, so the pressure is higher at the resistor and the λ transition occurs at a lower temperature. The difference is about 5 μK and is taken into account in calculations of $T - T_\lambda$. The power to this resistor is off when spectra are recorded.

IV. DATA ANALYSIS

$T - T_\lambda$ is not defined uniquely until the path of measurement is specified. For this purpose we let $\Theta \equiv T_\lambda - T$ as measured along an isobar. Figure 5 shows[50] the experimental path and a section of the λ line in the PT plane. Let the point
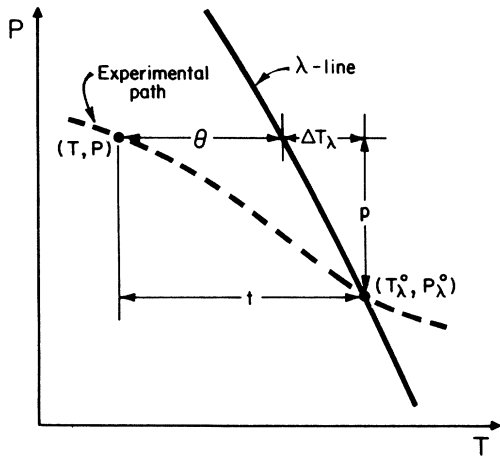
FIG. 5. Detail of the phase diagram of ^{4}He, showing the experimental path. t is $T_\lambda - T$ measured along the experimental path. Θ is $T_\lambda - T$ measured along an isobar.

FIG. 6. Four Brillouin spectra taken at $P_\lambda = 23.1$ bars near the λ transition of liquid ^{4}He. In the top spectrum the frequency shifts of first and second sound are marked. For second sound, zero-frequency shift is at the center of the marked free spectral range (149.7 MHz). The instrumental linewidth (3 MHz) is also shown.

$(T_\lambda^0, P_\lambda^0)$ be the intersection of the experimental path with the λ line. The germanium resistor gives $t = T_\lambda^0 - T$, while the capacitor gives $p = P - P_\lambda^0$. ΔT_λ can be determined from the known slope of the λ line.[51] Then we have $\Theta = t + (\partial T/\partial P)_\lambda p$. A typical set of values at 23 bars is $t = 1.1$ mK, $p = 0.023$ bars, $\Theta = 0.75$ mK. Where p is sizable, the full equation for $T_\lambda(P)$ is used to determine ΔT_λ. The conversion from t to Θ is appropriate because the important quantities (intensities, frequency shifts, linewidths) vary much more rapidly as functions of Θ than as functions of P.

Although the experimental path is very nearly an isochore, there are two reasons why small deviations occur. Small portions of the sample volume (0.2 cm^3) are at various temperatures between 2 and 300 K. In addition, the absorption of laser power causes small inhomogeneous regions in the cell. These regions are near the laser windows and the outer apertures where the power is absorbed. The small heat and mass currents generated there do not reach the scattering volume because the silver disks promote thermal homogeneity and the apertures restrict mass flow; but the density is not precisely uniform throughout the cell. As a result of these two situations, changes in T or P have small but measurable effects on the density in the scattering region when operating very close to T_λ. Notice that the conversion from t to Θ does not depend upon the experimental path being an isochore.

The scattering wave vector is given by Eq. (1). Although the index of refraction of helium depends on its density, the change in n_r between the two isochores of this experiment is only 0.0008. The
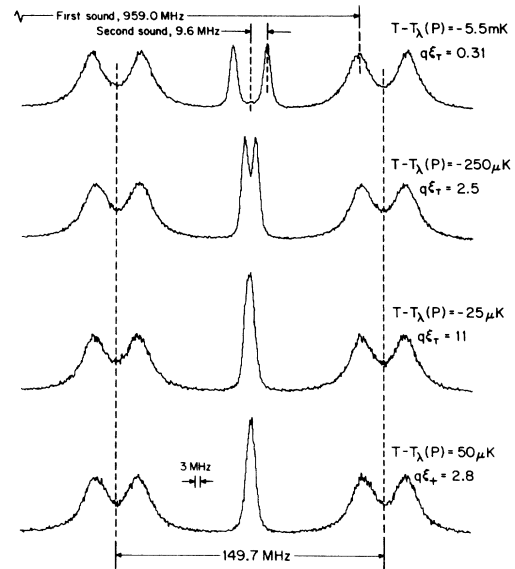
scattering angle varied a total of 0.01 rad in the several experimental runs but was measured to better than 0.001 rad during each run. The average scattering angle was $\frac{1}{2}\pi$, and the wave vector was 1.79×10^5 cm^{-1} on both isochores.

Since the Fabry-Perot is a filter with a periodic transmission, all the information available is contained in one free spectral range (FSR), the size of which is determined by the length of the Fabry-Perot. If the transmission is swept through more than one FSR, the information is repeated. This point is illustrated in Fig. 6, which displays four spectra obtained with $P_\lambda = 23.1$ bars. In the top trace, one sees two peaks for first sound and two for second sound in one FSR. The second sound peaks are shifted less than $\frac{1}{4}$ FSR at all temperatures of this experiment. Zero-frequency shift for them is the center of the FSR shown. Although the first sound peaks appear to be shifted by less than $\frac{1}{2}$ FSR, the actual shift is about 6.4 FSR. The lower spectra in Fig. 6 show successively warmer temperatures, and the second sound portions of these spectra follow the trend shown in Fig. 1.

The measured spectrum differs from $S_1 + S_2$ due to three effects. First, the spectrometer has a finite resolution. The line shape of the spectrometer is measured by introducing laser light directly into the instrument. This instrumental profile must be convolved with the theoretical spectra before they are compared with the data.

Second, a small distribution of wave vectors is

accepted by the spectrometer at a given mean scattering angle. The effect on second sound is negligible, but, because the frequency shift of first sound is large, its spectrum is affected by this relatively narrow distribution of q. The laser beam has a Gaussian angular distribution of wave vectors, and the collection optics[52] of the spectrometer have been designed to collect a rectangular distribution of scattering angles. The width of the distribution due to the two effects is about 0.006 rad and would give first sound an apparent full width of 3 MHz even if its intrinsic width were zero.

Finally, the photomultiplier gives dark counts at a rate of 1/sec, and some light is elastically scattered by the cell. To take all three effects into account, the measured spectra are compared with the following form:

$$S_T(\omega) = I(\omega) * [S_1(q, \omega) * G(\omega) * R(\omega) + S_2(q, \omega)]$$
$$+ I_s I(\omega) + D . \qquad (19)$$

Here $*$ represents a convolution, $I(\omega)$ is the normalized instrumental profile, $G(\omega)$ is a normalized Gaussian with standard deviation $\sigma = 8.1 \times 10^{-4} \omega_1$, $R(\omega)$ is a normalized rectangle with a full width $\Delta \omega = 2.7 \times 10^{-3} \omega_1$, D is the dark count, and I_s is the contribution from stray light. A computer program performs the convolutions, and, if there are parameters to optimize, the program finds the values which minimize the weighted rms deviation between the theoretical and measured spectra. Where Eqs. (5) and (7) are used for S_1 and S_2, their relative intensities are permitted to vary.

I_s is due to geometrical effects independent of temperature. It is measured in the normal fluid at the temperature where the coefficient of thermal expansion is zero. S_2 is zero at that temperature because $\gamma - 1 = 0$. Far below T_λ, where the stray light is clearly separated from second sound, I_s can be fit by the program. The two methods for determining I_s agree within their errors.

V. RESULTS

We begin this section with results for the intensity ratio I_2/I_1. The experimental determination of this ratio is not particularly sensitive to the spectral shape of S_1 and S_2, and it provides a simple indication of departures from hydrodynamics. The remainder of the section concerns the spectral shape of S_2. Outside the critical region the measured spectra are fit to the hydrodynamic form, and the relevant thermodynamic quantities are extracted. Next, a simple model form for S_2 is introduced and used to parametrize the experimental spectra over the entire range of temperatures studied. Finally, the measured spectra are compared directly with spectra calculated for the symmetric planar-spin model.

The experiments were carried out along two separate paths which are nearly isochores: the one defined by $P_\lambda = 23.1$ bars corresponds to $T_\lambda = 1.880$ K and $\rho = 0.175$ g/cm^3; the other, for which $P_\lambda = 28.5$ bars, has $T_\lambda = 1.792$ K and $\rho = 0.179$ g/cm^3. The wave vector of the fluctuations is $q = 1.79 \times 10^5$ cm^{-1}.

A. Intensity ratio

Previous light-scattering experiments[24,26] have found that the Landau-Placzek ratio I_2/I_1 falls below the hydrodynamic value $\gamma - 1$ close to T_λ. $\gamma - 1$ has a weak divergence at T_λ, while I_2/I_1 goes through a broad maximum at a temperature below T_λ. The total scattered intensity[23] has a similar behavior. The deviation of I_2/I_1 from $\gamma - 1$ is due to nonhydrodynamic effects associated with the critical region. The behavior of I_2/I_1 in the critical region has been discussed by Stephen[34]; however, there is as yet no calculation which reproduces the full temperature dependence of I_2/I_1, in particular, its final decrease as T_λ is approached from below.

Figure 7 shows our results for the Landau-Placzek ratio I_2/I_1. They were obtained by fitting the experimental spectra to Eq. (19) with S_1 given by Eq. (4) and S_2 represented by a two-Lorentzian model which will be discussed below. In the hydrodynamic region a similar fit was carried out using Eq. (7) for S_2; the resulting values for I_2/I_1 were the same as those in Fig. 7 to within the experimental precision. The solid line in the figure is $\gamma - 1$. Recent measurements of the thermal expansion coefficient[53] have indicated that the specific-heat data,[50] to which some of the previous light scattering results were compared, was slightly in error at pressures above 20 bars. Therefore the $\gamma - 1$ used here was obtained from the thermal-expansion data as explained in the appendix.

An interesting feature of our intensity ratio measurements is that below T_λ, I_2/I_1 appears to rise above $\gamma - 1$ before it rolls over. Earlier measurements of I_2/I_1 in this laboratory at 25.4 bars are numerically consistent with values obtained by interpolation between the two pressures shown in Fig. 7. However, when that data were published[24] they were compared with thermodynamic values[54] of $\gamma - 1$, which are now known to be too high near T_λ; consequently, in Fig. 2 of Ref. 24, $\gamma - 1$ was everywhere equal to or above the measured I_2/I_1. A subsequent comparison of the same I_2/I_1 data with values of $\gamma - 1$ obtained from the specific-heat data of Ahlers[50] showed a behavior qualitatively similar to that of Fig. 7, but with the maximum
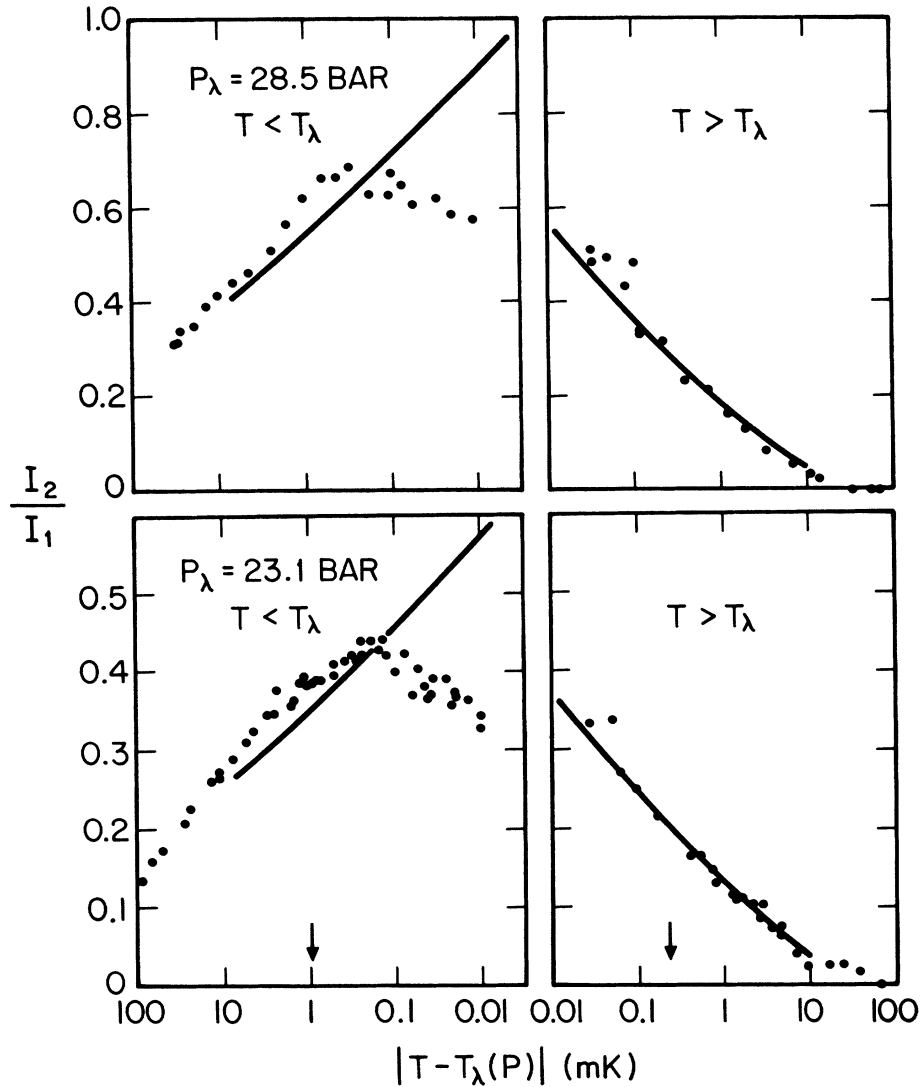
FIG. 7. Intensity ratio I_2/I_1. The solid lines give values of $\gamma-1$ calculated from the thermal-expansion coefficient. The arrows indicate the temperatures at which $q\xi = 1$ for a pressure of 23.1 bars.

overshoot of I_2/I_1 above $\gamma - 1$ being somewhat greater than found here. Finally, when the data at 25.4 bars is compared with the current best estimate of $\gamma - 1$, obtained from the thermal expansion, the overshoot is quantitatively, as well as qualitatively, consistent with the data in Fig. 7.

The situation with regard to this overshoot is still not clear, however. O'Connor $et\ al.$ working at 18.24 bars found no significant rise of I_2/I_1 above $\gamma - 1$ over the same range of temperatures. Their $\gamma - 1$ was based on Ahlers's specific-heat data,[50] and we find that the more accurate $\gamma - 1$ calculated from the thermal expansion gives essentially the same values at this pressure. They also carried out a few measurements at 26 bars on

which they did not elaborate other than to say that they found good agreement with Ahlers's data for $\gamma - 1$ as long as $T - T_\lambda < -0.3$ mK. It should also be pointed out that in Stephen's theory of the intensity ratio,[34] based on Ornstein-Zernike corrections to the hydrodynamic theory, I_2/I_1 does not exceed $\gamma - 1$.

O'Connor $et\ al.$ suggest that our measured values of I_2/I_1 may be too high due to the inclusion of some stray elastically scattered light in the signal attributed to I_2. However, figures such as Figs. 8 and 14(a) indicate that a small amount of elastically scattered light, if present, can easily be resolved, at least for $T - T_\lambda < -1$ mK, and is accounted for separately in Eq. (19). In fact, when
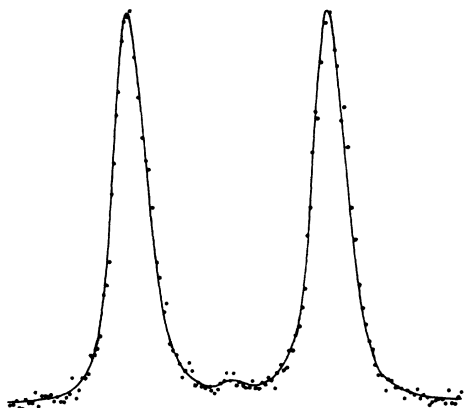
FIG. 8. Central portion of a spectrum taken at P_λ = 23.1 bars, $T - T_\lambda = -8$ mK. The solid line is the best fit to the hydrodynamic form.

I_2/I_1 is fixed at $\gamma - 1$ in this region, the rms deviations of the best fits to the spectra increase by about 10%, even when the intensity of the stray light is allowed to vary. Remember that S_2 occupies at most $\frac{1}{3}$ of the FSR, while the rms deviation is calculated for the entire FSR. It follows that the increase in the deviation caused by forcing I_2/I_1 to equal $\gamma - 1$ is much larger than 10% in the vicinity of S_2.

B. Hydrodynamic spectra

The hydrodynamic form for S_2 below T_λ [Eq. (7)] contains the frequency shift ω_2 and the two contributions to the linewidth Γ_ζ and Γ_κ. These three parameters were determined from fits to the measured spectra for $T - T_\lambda < -1$ mK. The quality of these fits is indicated in Fig. 8 which shows the central portion of a spectrum taken at $P_\lambda = 23.1$ bars and $T - T_\lambda = -8$ mK.
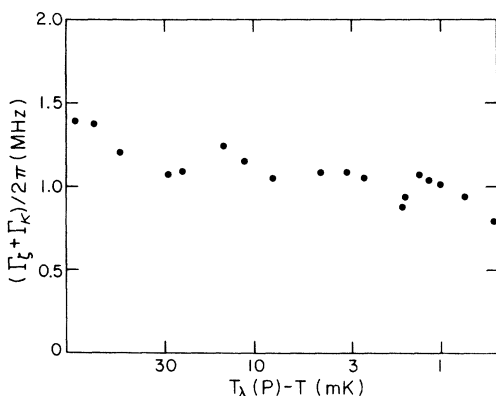

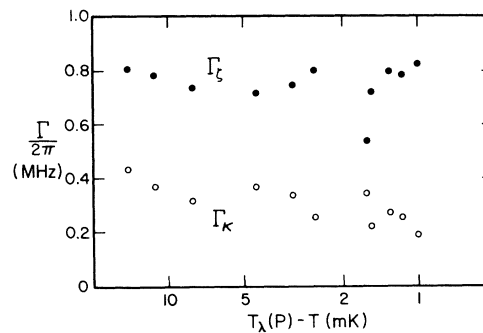FIG. 9. Half width entering the hydrodynamic form for the second-sound spectrum at a pressure of 23.1 bars.

FIG. 10. Two separate contributions to the hydrodynamic linewidth at a pressure of 23.1 bars.

At 23.1 bars the measured ω_2 equals qu_2 calculated using the low-frequency velocity data of Greywall and Ahlers,[40] but at 28.5 bars ω_2 exceeds qu_2 by about 2% in the region -10 mK $< T - T_\lambda < -1$ mK. The results at 28.5 bars may indicate dispersion in the high-frequency velocity; however, the data are not conclusive since the difference between the velocities is roughly equal to the combined uncertainties in the two experiments.

Figure 9 shows the data for the total second sound linewidth, $\Gamma_\zeta + \Gamma_\kappa$, at 23.1 bars. The significance of these results will be discussed in Sec. V C. Figure 10 gives the two components Γ_ζ and Γ_κ separately. Over the temperature region covered in the figures, Γ_ζ is roughly twice Γ_κ. A similar relationship was observed at 28.5 bars. This ratio is in good agreement with the results of Winterling et al.[24] at 25.4 bars who found $\Gamma_\zeta/(\Gamma_\zeta + \Gamma_\kappa) = 0.6 \pm 0.1$. It is at variance, however, with the result of Vinen et al.[27] at 20.2 bars who found $\Gamma_\zeta/\Gamma_\kappa < 0.2$. To investigate the significance of this discrepancy, we tested the sensitivity of our spectral fits to the value of the ratio $\Gamma_\zeta/\Gamma_\kappa$. Some of the results are shown in Fig. 11(a) which represents on an enlarged scale the region near $\omega = 0$ from the trace of Fig. 8. The solid line is the best fit with no restrictions ($\Gamma_\zeta/2\pi = 0.74$ MHz, $\Gamma_\kappa/2\pi = 0.32$ MHz). The dashed line is the best fit with the restriction $\Gamma_\zeta = 0.2\Gamma_\kappa$ and with the stray light I_s fixed at its measured value of $2 \times 10^{-3} I_1$. The dotted line is the best fit with the restriction $\Gamma_\zeta = 0.2\Gamma_\kappa$ and with I_s allowed to vary as a free parameter. This figure shows that our results do not support the ratio $\Gamma_\zeta/\Gamma_\kappa < 0.2$ found by Vinen et al.[27] and that the discrepancy cannot be due to stray light.

In the hydrodynamic region above T_λ, S_2 should be a simple Lorentzian line [Eq. (9)]. The measured spectra are consistent with this form, and we have determined the linewidth. The discussion of this linewidth is contained in Sec. V C.
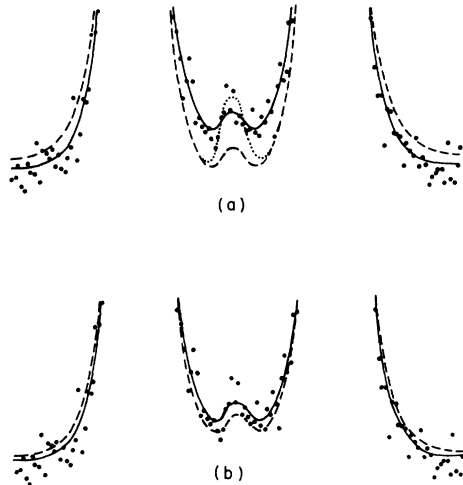
FIG. 11. Detail of various fits to the spectrum of Fig. 8. The solid line is the best fit to the hydrodynamic form. (a) The dashed line is the best fit to the hydrodynamic form with the restrictions: $\Gamma_\zeta/\Gamma_\kappa = 0.2$, $I_S/I_1 = 0.002$. The dotted line is the fit with the restriction: $\Gamma_\zeta/\Gamma_\kappa = 0.2$. (b) The dashed line is the fit to the two-Lorentzian model.

C. Two-Lorentzian model

Inside the critical region near T_λ there is no reason to expect that the hydrodynamic form for S_2 will be correct. We see evidence for this above T_λ: the quality of the single Lorentzian fit to our spectra decreases when $T - T_\lambda < 0.1$ mK. The effect below T_λ is more subtle. If we try to use Eq. (7) to represent S_2 closer than 1 mK to T_λ, the three-parameter $(\omega_2, \Gamma_\zeta, \Gamma_\kappa)$ fit produces spurious results. The values of Γ_ζ and Γ_κ are scattered because the measured spectrum is insensitive to $\Gamma_\zeta/\Gamma_\kappa$ near T_λ. Furthermore, the results are misleading because Γ_ζ and Γ_κ cease to have the customary physical meaning in terms of second sound damping when they are about equal to ω_2.

In order to characterize our measured spectra in both the hydrodynamic and the critical regions, we have chosen a simple two-parameter model for S_2. It consists of a pair of Lorentzians of equal area and equal half width Γ_2, displaced by $\pm\omega_2$ from $\omega = 0$:

$$S_2(\omega) = \frac{I_2\Gamma_2}{2\pi}\left(\frac{1}{(\omega - \omega_2)^2 + \Gamma_2^2} + \frac{1}{(\omega + \omega_2)^2 + \Gamma_2^2}\right). \quad (20)$$

This two-Lorentzian model reduces to the exact hydrodynamic spectrum above T_λ when $\omega_2 = 0$. In the hydrodynamic region below T_λ, it gives a very good, but not perfect, fit to our measured spectra. Figure 11(b) compares the best fit using this form with the best fit using the hydrodynamic

form. Although the two-Lorentzian model (dashed line) does not represent the experimental trace quite as well as does the hydrodynamic form, the fitted values of ω_2, Γ_2, and I_2 are the same in the two cases. The parameters fitted by the two forms only begin to differ for $T - T_\lambda > -1$ mK. The parameters of the two-Lorentzian model vary smoothly with temperature as T_λ is approached more closely, whereas the hydrodynamic form becomes unreliable. We certainly do not propose that this model is the exact spectral form in the critical region, but we use it as a convenient and consistent method of parametrizing the spectra in all temperature regions.

Figure 12 shows the fitted values for the frequency shift ω_2 using the two-Lorentzian model and the shift expected from the low-frequency velocity data of Greywall and Ahlers.[40] Notice that very close to T_λ $\omega_2/2\pi$ deviates from $qu_2/2\pi$ and approaches a temperature-independent value of about 1.5 MHz. This is consistent with the prediction of dynamic scaling that S_2 approaches some temperature-independent limiting from near T_λ. A finite ω_2 at T_λ also supports the physical
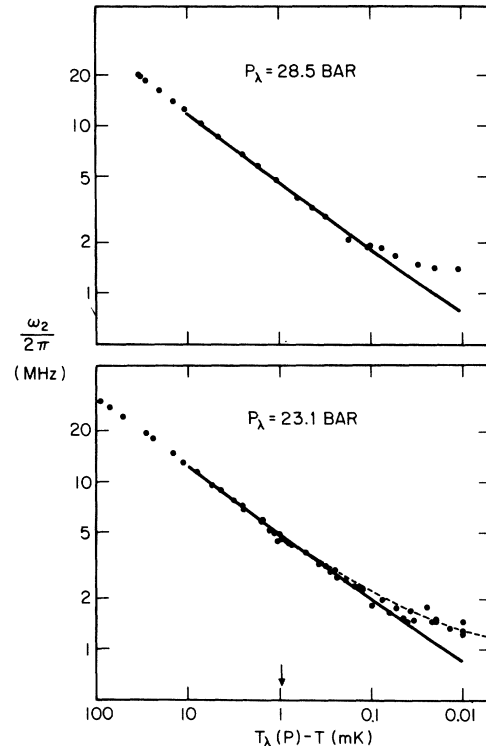

FIG. 12. Second-sound frequency shift for the two-Lorentzian model. The solid lines represent $qu_2(T)$ with u_2 taken from Ref. 40. The dashed curve is the prediction of the planar-spin model. The arrows indicate the temperatures at which $q\xi = 1$ for a pressure of 23.1 bars.

picture of Ferrell et al.[6] that for a nonzero wave vector the superfluid density ρ_s (and therefore u_2) can be considered finite at T_λ. Above T_λ, ω_2 decreases again until it reaches a background noise level by the point where $q\xi_+ \sim 1$.

Figure 13 contains our measured values of Γ_2. Note that the vertical scale is linear. It shows that the damping of the critical mode is roughly independent of temperature over four orders of magnitude in reduced temperature ϵ below T_λ and three orders of magnitude in ϵ above T_λ. This unexpected behavior below T_λ was first observed by Winterling et al.[24,25] and subsequently confirmed by Vinen et al.[27] Recall that Tyson's low-frequency data for $T < T_\lambda$ seemed to confirm the dynamical

scaling prediction of a divergent damping in the hydrodynamic region. Equations (8) and (16) show that Γ_2 is expected to vary as $u_2 \xi q^2$. We have extrapolated Tyson's data by q^2, and we have adjusted it to our pressures by using the measured pressure dependence of u_2,[40] and by assuming that $\xi(\epsilon)$ is independent of pressure.[41] The resulting Γ_2, which is plotted in Fig. 13, shows a strong temperature dependence and crosses our values at $T - T_\lambda \sim -10$ mK. Since $q\xi_T \sim 0.2$ at this point, one would have expected hydrodynamic behavior in that vicinity. Other effects of the critical region (the maximum of I_2/I_1 and the limiting behavior of ω_2) occur much closer to T_λ.

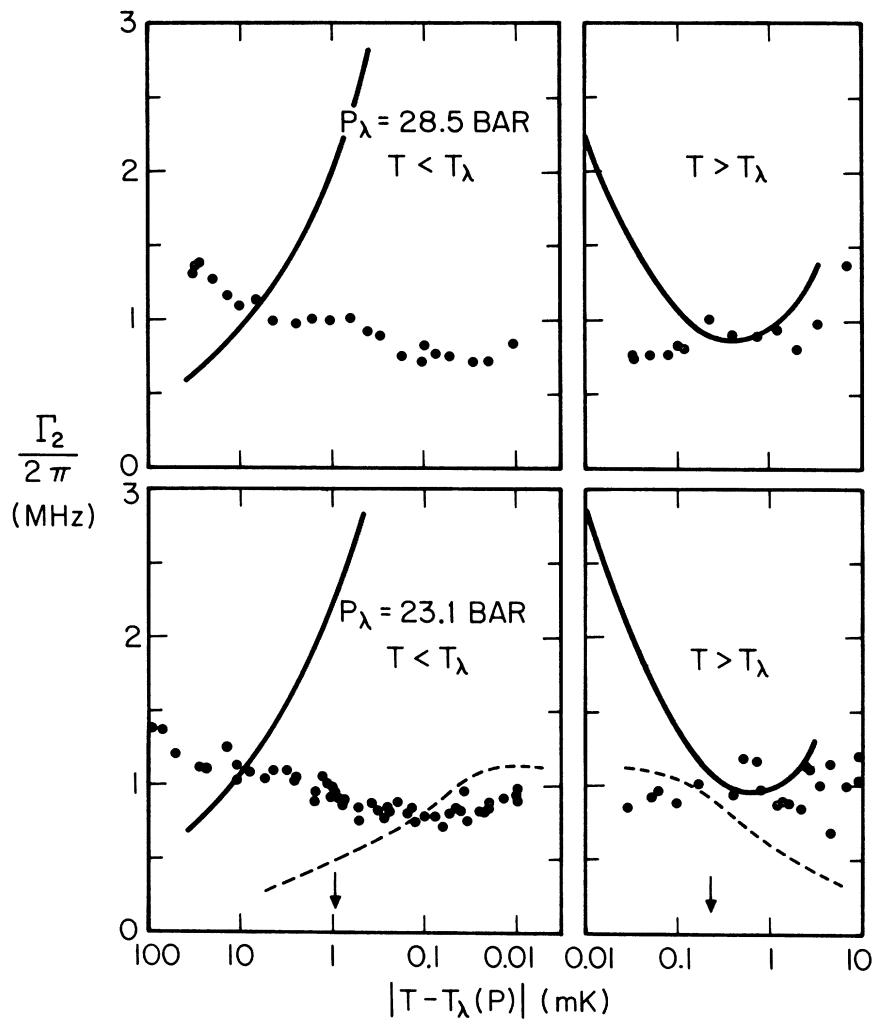The constant linewidth above T_λ is in agreement

FIG. 13. Half width for the two-Lorentzian model. For $T < T_\lambda$ the solid lines are based on q^2 extrapolations of the low-frequency data of Tyson, Ref. 9. For $T > T_\lambda$ the solid lines represent $\kappa q^2 (\rho C_p)^{-1}$. The dashed curve is the prediction of the planar-spin model. The arrows indicate the temperatures at which $q\xi = 1$ for a pressure of 23.1 bars.

with the results of Vinen *et al.*[27] The expected half width $\kappa q^2 (\rho C_P)^{-1}$ is plotted along with the data. κ is taken from the data of Kerrisk and Keller[55] and Ahlers,[56] and C_P is also from Ahlers's data.[50] The deviation between the data and the calculated

linewidth is not surprising above T_λ because the difference first appears at $T - T_\lambda \approx 0.2$ mK, where $q\xi_+ \sim 1$. Notice that the linewidth determined by fitting to the two-Lorentzian model varies smoothly and continuously through T_2.
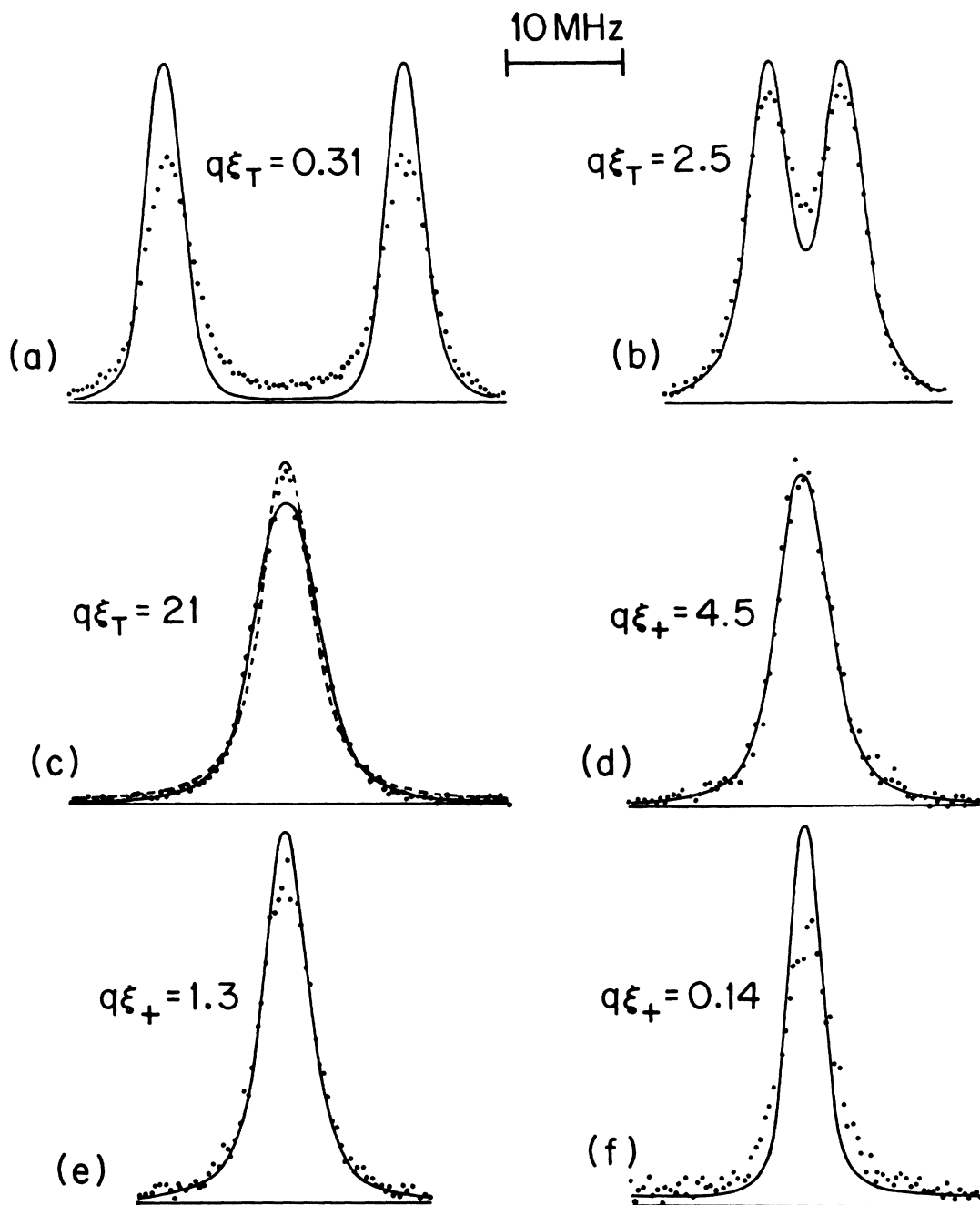
FIG. 14. Central portion of spectra recorded at $P_\lambda = 23.1$ bars. The contributions of first sound, stray light, and dark count have been removed from the spectra. In order, the temperatures are $(T - T_\lambda)$: $-5.5, -0.25, -0.01, 0.025, 0.16$, 4.5 mK. The solid lines are theoretical spectra predicted by the planar-spin model convolved with the line shape of our instrument. The dashed line in (c) is the fit to a single Lorentzian.

D. Symmetric planar-spin model

Very near T_λ our fitted parameters indicate that the second-sound peaks have full widths of $2\Gamma_2/2\pi$ ≈ 2 MHz and are split by $2\omega_2/2\pi = 2.7$ MHz. These parameters are comparable to the full width at half height (2.9 MHz) of the instrumental profile $I(\omega)$. Consequently, we are unable to determine the limiting form of the structure factor directly. We can, however, compare our spectra with theoretical calculations of $S_2(q, \omega)$ by convolving the theoretical spectra with $I(\omega)$. Hohenberg, Siggia, and Halperin[28] have calculated $S_2(q, \omega)$ in the symmetric planar-spin model with no adjustable parameters. Spectra calculated from this theory and convolved with $I(\omega)$ are compared with experimental traces in Fig. 14. The contributions from first sound, stray light, and dark count have been subtracted from the experimental spectra in that figure. In each case, the experimental and theoretical curves have been adjusted to have equal areas. In comparing these spectra, one must remember that about half the breadth is due to the instrument.

In the hydrodynamic region above T_λ the theoretical shape of S_2 is Lorentzian. For the conditions of Fig. 14(f) the theory predicts a linewidth $\Gamma/2\pi$ of about 0.40 MHz. The comparison in Fig. 14(f) shows that this predicted width is too small. (Note that the theoretical curve, of equal area, is too high near $\omega = 0$ and falls too rapidly in the tails.) However, we find that this trace can be fit by a single Lorentzian whose width, from Fig. 13, is about 1.1 MHz.

In Fig. 14(e) the theory begins to deviate from a Lorentzian line shape, but the effect is too small to resolve. The theoretical width is still too small. Figure 14(d) shows a very good agreement between theory and experiment. This is true not only of the width, but of the shape as well. The theory, before convolution with the instrument, is decidedly non-Lorentzian (refer to Fig. 2 of Ref. 28). The line shape is flatter near the maximum and falls more rapidly in the tails than a Lorentzian. An indication of the sensitivity of our measurements to the line shape in this region is given by the fact that the best fit to the two-Lorentzian model gives $\omega_2/2\pi = 1$ MHz and $\Gamma_2/2\pi = 1$ MHz. The model is attempting to approximate the "squarer-than-Lorentzian" shape of the intrinsic line by using two Lorentzians with a finite separation.

In Fig. 14(c), which is just below T_λ, the theory again matches the experiment surprisingly well; only a small difference is seen at $\omega = 0$. Here, as in Fig. 14(d), the theory is non-Lorentzian (see Fig. 1). The best fit to a single Lorentzian, shown as a dashed line, is not as good. The single

Lorentzian fit is too narrow near half height, and it is too high in the tails. The two-Lorentzian model, on the other hand, fits the data almost as well as the solid line because it broadens the fit near half height (by increasing ω_2) and lowers the fit far from the center (by decreasing Γ_2).

Figure 14(b) is notable because two peaks are resolved even though $q\xi_T = 2.5$. In fact, two peaks are experimentally resolved even at $q\xi_T = 4$. The theory is once again too narrow in Fig. 14(b). In Fig. 14(a), which is in the hydrodynamic region below T_λ, the theory is much too narrow and has too little weight at $\omega = 0$. At that temperature, $\Gamma_2/2\pi = 1$ MHz, while the half width of the theory is 0.3 MHz.

Our experiments show that the limiting linewidth near T_λ is given quite well by the symmetric planar-spin model. We also see evidence for a "squaring off" of the limiting spectral shape which is an important feature of that model. However, as the hydrodynamic region is approached on either side of T_λ, the symmetric planar-spin model predicts linewidths which are too narrow. To exhibit this behavior in a quantitative manner, we have used our fitting programs to approximate these theoretical spectra by the two-Lorentzian model (in this case, of course, no instrumental profile is involved). The best-fit values for ω_2 and Γ_2 are shown in Figs. 12 and 13 by dashed lines. In the hydrodynamic region below T_λ, the linewidth from this theory has the dynamical scaling temperature dependence, but its magnitude is smaller by a factor of 5 than the extrapolation of Tyson's low frequency measurements. In this same region the symmetric planar-spin model gives a value of 0.36 for $\Gamma_\zeta/\Gamma_\kappa$,[57] which is inconsistent with our measured value of about 2. It is also interesting to note that in the hydrodynamic region above T_λ the linewidth of the calculated spectra is less than $\kappa q^2/\rho C_P$. The experimental traces are consistent with $\Gamma \approx \kappa q^2/\rho C_P$.

APPENDIX

To obtain the relation between $\gamma - 1$ and α_P, we make use of the general expression for the ratio of specific heats

$$\gamma \equiv C_P/C_V = 1 + \alpha_P^2 T/\rho C_V \beta_T , \qquad (A1)$$

where C_V is the specific heat per unit mass. We now eliminate C_V and β_T by using two Pippard-Buckingham-Fairbank relations.[41] These relations are derived from the total differentials of thermodynamic parameters (such as volume) by choosing a particular path relating the independent thermodynamic variables. For example

$$dV = \left(\frac{\partial V}{\partial T}\right)_P dT + \left(\frac{\partial V}{\partial P}\right)_T dP \qquad (A2)$$

gives

$$\frac{1}{V}\left(\frac{dV}{dT}\right)_t = \alpha_P + \beta_T \left(\frac{dP}{dT}\right)_t , \qquad (A3)$$

where t indicates the relation between T and P. If, for instance,

$$t = T - T_\lambda(V) = \text{const} \qquad (A4)$$

is the relation between P and T, then $(dV/dT)_t$ is given by the derivative along the λ line $(\partial V/\partial T)_\lambda$,

and $(dP/dT)_t$ can be approximated by $(\partial P/\partial T)_\lambda$. Substituting, we find

$$\alpha_\lambda \equiv \frac{1}{V}\left(\frac{\partial V}{\partial T}\right)_\lambda \approx \alpha_P + \beta_T \left(\frac{\partial P}{\partial T}\right)_\lambda . \qquad (A5)$$

The total differential of entropy, using T and V as independent variables, gives another relation

$$\rho \frac{C_V}{T} \approx \rho \left(\frac{\partial S}{\partial T}\right)_\lambda - \frac{\alpha_\lambda \alpha_P}{\beta_T} . \qquad (A6)$$

Using Eqs. (A5) and (A6) in Eq. (A1), we obtain

$$\gamma - 1 = \frac{-\alpha_P}{\alpha_\lambda}\left[1 + \rho\left(\frac{\partial S}{\partial T}\right)_\lambda \left(\frac{\partial T}{\partial P}\right)_\lambda \left(\frac{1}{\alpha_P} - \frac{1}{\alpha_\lambda}\right)\right]^{-1} . \qquad (A7)$$

The approximations are all contained in the second term in the brackets. Below T_λ, that term is about 0.25, and the small errors due to the approximations have a reduced effect on $\gamma - 1$. Above T_λ, the term is as large as 0.9, so the approximations could have a larger effect on $\gamma - 1$. The quantities α_λ and $(\partial T/\partial P)_\lambda$ are taken from Kierstead,[51] $(\partial S/\partial T)_\lambda$ from Ahlers,[50] and α_P from Mueller et al.[58] Above T_λ, this calculation gives values of $\gamma - 1$, which vary only slightly from those of Ref. 50, while below T_λ at 23 bars the values calculated here are several percent higher.

---

[1] See, for example, H. E. Stanley, *Introduction to Phase Transitions and Critical Phenomena* (Oxford University, New York, 1971).

[2] The importance of the index n in the theory of critical phenomena is emphasized in the review article by M. E. Fisher, Rev. Mod. Phys. 46, 597 (1974).

[3] H. Y. Lau, L. M. Corliss, A. Delapalme, J. M. Hastings, R. Nathans, and A. Tucciarone, Phys. Rev. Lett. 23, 1225 (1969); A. Tucciarone, H. Y. Lau, L. M. Corliss, A. Delapalme, and S. M. Hastings, Phys. Rev. B 4, 3206 (1971).

[4] M. P. Schulhof, P. Heller, R. Nathans, and A. Linz, Phys. Rev. Lett. 24, 1184 (1970); Phys. Rev. B 4, 2254 (1971).

[5] H. L. Swinney and D. L. Henry, Phys. Rev. A 8, 2586 (1973).

[6] R. A. Ferrell, N. Menyhard, H. Schmidt, F. Schwabl, and P. Szepfalusy, Ann. Phys. (N.Y.) 47, 565 (1968).

[7] B. I. Halperin and P. C. Hohenberg, Phys. Rev. 177, 952 (1969).

[8] L. P. Kadanoff, in *Critical Phenomena*, edited by M. S. Green (Academic, New York, 1971).

[9] J. A. Tyson, Phys. Rev. Lett. 21, 1235 (1968).

[10] J. A. Tyson and D. H. Douglass, Jr., Phys. Rev. Lett. 21, 1308 (1968).

[11] L. Van Hove, Phys. Rev. 95, 249 (1954).

[12] P. C. Hohenberg, in *Critical Phenomena*, edited by M. S. Green (Academic, New York, 1971).

[13] V. L. Ginzburg, J. Phys. USSR 6, 305 (1943).

[14] W. F. Vinen, J. Phys. C 4, L287 (1971).

[15] P. C. Hohenberg, J. Low Temp. Phys. 11, 745 (1973).

[16] R. L. St. Peters, T. J. Greytak, and G. B. Benedek, Opt. Commun. 1, 412 (1970).

[17] E. R. Pike, J. M. Vaughan, and W. F. Vinen, J. Phys. C 3, L40 (1970).

[18] E. R. Pike, J. M. Vaughan, and W. F. Vinen, Phys. Lett. A 30, 373 (1969).

[19] C. J. Palin, W. F. Vinen, E. R. Pike, and J. M. Vaughan, J. Phys. C 4, L225 (1971).

[20] D. A. Rockwell, R. F. Benjamin, and T. J. Greytak, J. Low Temp. Phys. 18, 389 (1975).

[21] G. Winterling, F. S. Holmes, and T. J. Greytak, in *Low Temperature Physics–LT13*, edited by K. D. Timmerhaus, W. J. O'Sullivan, and E. F. Hammel (Plenum, New York, 1974), Vol. I, p. 537.

[22] W. F. Vinen, C. J. Palin, and J. M. Vaughan, Ref. 21., p. 524; J. M. Vaughan, W. F. Vinen, and C. J. Palin, Ref. 21, p. 532.

[23] C. J. Palin, W. F. Vinen, and J. M. Vaughan, J. Phys. C 5, L139 (1972).

[24] G. Winterling, F. S. Holmes, and T. J. Greytak, Phys.

Rev. Lett. 30, 427 (1973).

[25]G. Winterling, J. Miller, and T. J. Greytak, Phys. Lett. A 48, 343 (1974).

[26]J. T. O'Connor, C. J. Palin, and W. F. Vinen, J. Phys. C 8, 101 (1975).

[27]W. F. Vinen, C. J. Palin, J. M. Lumley, D. L. Hurd, and J. M. Vaughan, in Low Temperature Physics— LT14, edited by M. Krusius and M. Vuorio (North-Holland, Amsterdam, 1975), Vol. I, p. 191.

[28]P. C. Hohenberg, E. D. Siggia, and B. I. Halperin, Phys. Rev. B 14, 2865 (1976).

[29]L. Onsager, Phys. Rev. 38, 2265 (1931).

[30]R. D. Mountain, Rev. Mod. Phys. 28, 205 (1966).

[31]I. M. Khalatnikov, Introduction to the Theory of Superfluidity (Benjamin, New York, 1965).

[32]W. F. Vinen, in Physics of Quantum Liquids, 1970 Tokyo Summer Lectures in Theoretical and Experimental Physics, edited by R. Kubo and F. Takano (Syokabo, Tokyo, 1971).

[33]F. S. Holmes, Ph.D. thesis (MIT, 1973) (unpublished).

[34]M. J. Stephen, in The Physics of Liquid and Solid Helium, edited by K. H. Bennemann and J. B. Ketterson (Wiley, New York, 1976), Part I, Chap. 4.

[35]H. H. Kretzen and J. J. Mikeska, Phys. Lett. A 43, 525 (1973).

[36]B. D. Josephson, Phys. Lett. 21, 608 (1966).

[37]J. A. Tyson and D. H. Douglass, Jr., Phys. Rev. Lett. 17, 472 (1966).

[38]J. R. Clow and J. D. Reppy, Phys. Rev. Lett. 16, 887 (1966).

[39]R. Williams, S. E. A. Bearer, J. C. Fraser, R. S. Kagiwada, and I. Rudnick, Phys. Lett. A 29, 279 (1969).

[40]D. S. Greywall and G. Ahlers, Phys. Rev. Lett. 28, 1251 (1972); Phys. Rev. A 7, 2145 (1973).

[41]See the review article by G. Ahlers, in The Physics of Liquid and Solid Helium, edited by K. H. Bennemann and J. B. Ketterson (Wiley, New York, 1976), Part I, Chap. 2.

[42]G. Ahlers, Phys. Rev. Lett. 21, 1159 (1968).

[43]B. I. Halperin, P. C. Hohenberg, and E. D. Siggia, Phys. Rev. B 13, 1299 (1976).

[44]J. R. Miller, Ph.D. thesis (MIT, 1976) (unpublished).

[45]S. A. Collins and G. R. White, Appl. Opt. 2, 448 (1963).

[46]Coherent Radiation Model 52 Argon Ion Laser.

[47]B. Rossi, Optics (Addison-Wesley, Reading, Mass., 1957), Chap. 6.

[48]G. C. Straty and E. D. Adams, Rev. Sci. Instrum. 40, 1393 (1969).

[49]C. E. Chase, Phys. Fluids 1, 193 (1958).

[50]G. Ahlers, Phys. Rev. A 8, 530 (1973).

[51]H. A. Kierstead, Phys. Rev. 162, 153 (1967).

[52]D. S. Cannell, Ph.D. thesis (MIT, 1970) (unpublished).

[53]K. H. Mueller, F. Pobell, and G. Ahlers, Phys. Rev. Lett. 34, 513 (1975).

[54]Computed from compressibility data of E. R. Grilly, Phys. Rev. 149, 97 (1966).

[55]J. F. Kerrisk and W. E. Keller, Phys. Rev. 177, 341 (1969).

[56]G. Ahlers, in Proceedings of the Twelfth International Conference on Low Temperature Physics, edited by Eizo Kanda (Academic, Japan, 1971), p. 21.

[57]P. C. Hohenberg (private communication).

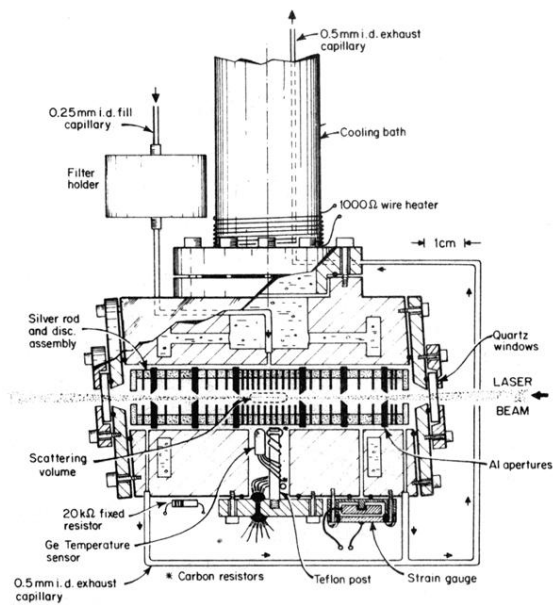[58]K. H. Mueller, G. Ahlers, and F. Pobell (unpublished).

FIG. 3. Scattering cell.